


Many-body effects in third harmonic generation of grapheneHabib Rostami ^{1,*} and Emmanuele Cappelluti ²¹*Nordita and Stockholm University, Roslagstullsbacken 23, SE-106 91 Stockholm, Sweden*²*Istituto di Struttura della Materia, CNR (ISM-CNR), 34149 Trieste, Italy* (Received 16 November 2020; revised 12 February 2021; accepted 1 March 2021; published 15 March 2021)

The low-energy (intra-band) range of the third harmonic generation of graphene in the terahertz regime is governed by the damping terms induced by the interactions. A controlled many-body description of the scattering processes is thus a compelling and desirable requirement. In this paper, using a Kadanoff-Baym approach, we systematically investigate the impact of many-body interaction on the third harmonic generation of graphene, taking elastic impurity scattering as a benchmark example. We predict the onset in the mixed inter- and intra-band regime of incoherent features driven by the interaction at four- and five-photon transition frequencies in the third harmonic optical conductivity with a spectral weight proportional to the scattering rate. We also show that in spite of the complex many-body physics, the purely intra-band term governing the limit $\omega \rightarrow 0$ resembles the constraints of the phenomenological model. We ascribe this agreement to the fulfilling of the conservation laws enforced by the conserving approach. However, the overlap with incoherent features and the impact of many-body-driven multiphoton vertex couplings severely limit the validity of phenomenological description.

DOI: [10.1103/PhysRevB.103.125415](https://doi.org/10.1103/PhysRevB.103.125415)**I. INTRODUCTION**

A simple dimensional analysis shows that the zero-temperature third harmonic response of clean graphene scales as $\sigma^{(3)} \sim 1/(\omega^3|\mu|)$ [1–5], where μ is the chemical potential and ω is the frequency of the incident field. Comparing it to the scaling of linear conductivity at low frequency, $\sigma^{(1)} \sim |\mu|/\omega$, we can thus expect a huge enhancement of the nonlinear optical response at low frequencies. Accordingly, there is a surge of experimental interest in exploring nonlinear optics of graphene and other two-dimensional materials in the terahertz frequency range. The effective three-dimensional third harmonic generation (THG) susceptibility of graphene with an effective thickness ~ 0.1 nm has been measured as 10^{-19} – 10^{-16} m²/V² [6–9] in the near-infrared and visible frequency range $\hbar\omega \sim 100$ – 500 THz, whereas in the terahertz range ($\hbar\omega \sim 1$ THz) a susceptibility as large as 10^{-9} m²/V² is obtained [10,11]. In these works, however, the nonlinear response was not related to multiphoton absorption and emission but rather to the underlying nonlinear dependence of the low-frequency intra-band linear conductivity on the electronic temperature ruled by the magnitude of the incident laser power [9,12,13]. The intrinsic role of multiphoton processes is thus completely missing in the interpretation of this experimental observation.

In common graphene, the terahertz frequency range, 1 THz ~ 4 meV, is much below the interband transition, $\hbar\omega \ll 2|\mu|$, and therefore the optical response is mainly governed by intra-band processes. Even in the low-doping regime, the terahertz-range interband transitions will be essentially Pauli blocked owing to temperature effects, charge-puddle formation, and many-body-induced band broadening. The intra-band response is very sensitive to the scattering processes which result in the momentum relaxation of quasiparticles. Therefore the many-body interaction is expected to have an unavoidable impact on the intra-band optical response of the Dirac fermions in graphene. A compelling study of nonlinear responses is usually a delicate and cumbersome task. Therefore the number of studies exploring many-body effects on the nonlinear optical response in a systematic way is quite limited [5,14–18]. A practical shortcut for including the impact of the scattering in the analysis is through a phenomenological relaxation rate Γ independent from energy and field [2,3]. This rough approximation may work qualitatively well in the high-doping and high-frequency ($|\mu|, |\hbar\omega| \gg \Gamma$) regime. However, even in high-quality graphene samples a scattering rate Γ not less than $\Gamma \approx 2$ – 5 THz was estimated in a wide range, $\mu \sim 0$ – 200 meV [19,20]. Therefore, in the terahertz range ($\hbar\omega \sim 1$ THz) we are rather in the regime $\hbar\omega < \Gamma$, questioning the validity of a constant- Γ model. Furthermore, in the low-frequency regime, vertex corrections to the linear ones are expected to be extremely relevant due to the proximity to the multiphoton self-generation [18].

The aim of this paper is to provide a compelling many-body approach for the nonlinear response of graphene and other two-dimensional Dirac systems in the terahertz frequency range, where the role of scattering is fundamentally important. We derive a conserving quantum theory based on the Kadanoff-Baym framework [21], which contains both the

*habib.rostami@su.se

self-energy and vertex correction effects on the same footing. Our theory is therefore consistent with conservation laws and the gauge invariance. To further preserve the gauge invariance and not violate the Ward identity, we employ a dimensional regularization [22,23] in the evaluation of momentum integrals in a Dirac model of graphene for which a high-energy cutoff is unavoidable. For the sake of simplicity, we only focus on the impact of disorder scattering within the self-consistent Born approximation (SCBA). However, our formal and technical scheme, i.e., the Kadanoff-Baym functional derivation and the diagrammatic structure, is valid also for scattering with phonons and other electrons in the system within a mean-field approximation. Most of our qualitative predictions are thus expected to be valid also for other types of scattering processes.

Our main results can be summarized as follows: (i) We predict the onset of four- and five-photon transitions in the third harmonic response of graphene. As a result of such four- and five-photon transitions, the THG of graphene is strongly enhanced in the intraband regime where $\hbar\omega$ is smaller than the three-photon transition edge. These transitions are intrinsically driven by the interaction with a spectral weight that scales with the magnitude of the one-particle scattering rate, revealing the intrinsic incoherent character. (ii) A strong impact of vertex corrections is revealed owing to the presence of many-body-induced two- and three-photon current vertices which are absent in noninteracting Dirac fermions in graphene. A crucial role in this regard is played, in particular, by the occurrence of the two-photon vertex self-generation in the intraband terahertz regime, close to the dc limit. (iii) In the extreme low-frequency limit, we find a good agreement of the pure intraband term in the presence of many-body effects with the phenomenological models, as the result of enforcing a conserving approach. Departures from this modeling are, however, also observed at relatively small scattering due to the onset of incoherent four- and five-photon transitions and the two-photon vertex self-generation. Our theoretical modeling can be generalized in a straightforward way to describe intraband THG in other two-dimensional materials such as transition-metal dichalcogenides (TMDs), homo- and heterobilayer systems, etc. The main challenges to be addressed in TMDs along these lines are as follows: the parabolic behavior for low electron or hole doping, related also to the appearance of a finite diamagnetic term; the sizable spin-orbit interaction; the possible relevance of other valleys (e.g., Γ , Q); and the fact that single-layer TMDs are noncentrosymmetric, resulting in a finite second-order response. Furthermore, the excitonic contribution in TMDs' optical response must be taken into account.

The rest of the paper is structured in five sections. In Sec. II, we introduce the conserving Kadanoff-Baym derivation employed to evaluate the nonlinear current within the Dirac model, and we introduce the elastic-impurity-induced self-energy. In Sec. III, we formally derive the many-body-induced multiphoton vertices based on self-consistent Bethe-Salpeter equations within the Kadanoff-Baym method. In Sec. IV we provide all of the analytical relations for the third-order response function using a diagrammatic quantum theory for THG in graphene and for generic two-dimensional Dirac systems. In Sec. V, we present our numerical results for the

real and imaginary parts of the third harmonic conductivity in graphene, and we discuss the onset of incoherent transition peaks, the impact of vertex renormalization, and the spectral features of pure intraband processes. Finally, in Sec. VI we provide a summary and conclusion.

II. MODEL AND METHOD

We use the Dirac Hamiltonian of low-energy carriers in graphene [24]

$$\hat{\mathcal{H}}_{\mathbf{k}} = \hbar v \hat{\sigma} \cdot \mathbf{k} - \mu_0 \hat{I}, \quad (1)$$

where \hat{I} is the identity matrix in the Pauli matrix space, \mathbf{k} is the in-plane momentum $\mathbf{k} = (k_x, k_y)$ measured with respect to the nodal point, μ_0 is the bare chemical potential, and $v \sim 10^6$ m/s is the Fermi velocity. Note that the Hamiltonian (1) includes the dependence both on the pseudospin sublattice degree of freedom and on the valley. More explicitly, we write $\hat{\sigma} = (\tau \hat{\sigma}_x, \hat{\sigma}_y)$, where $\hat{\sigma}_x, \hat{\sigma}_y$ stand for the Pauli matrices in the sublattice basis and $\tau = \pm$ accounts for the two inequivalent valleys in the Brillouin zone of graphene.

In the dipole approximation we can model light-matter interaction by applying the minimal coupling transformation $\hbar\mathbf{k} \rightarrow \hbar\mathbf{k} + e\mathbf{A}(t)$, where $\mathbf{A}(t)$ stands for an external vector potential and the corresponding electric field is given by $\mathbf{E}(t) = -\partial_t \mathbf{A}(t)$. For the sake of shortness the speed of light is set as $c = 1$. The inverse of the bare Green's function in the presence of the external vector potential thus reads [25,26]

$$\hat{G}_0^{-1}(1, 1'; \mathbf{A}) = \{i\partial_{t_1} - v\hat{\sigma} \cdot [-i\hbar\nabla_1 + e\mathbf{A}(1)] + \mu_0\} \times \delta(1 - 1'), \quad (2)$$

where we use the shorthand notation $1 \equiv (\mathbf{r}_1, t_1)$ for the space-time coordinate. In the presence of many-body scattering, it is useful to introduce an interacting Green's function:

$$\hat{G}(1, 1'; \mathbf{A}) = -i\langle \mathcal{T}[\hat{\psi}_{\mathcal{H}}(1)\hat{\psi}_{\mathcal{H}}^\dagger(1')] \rangle, \quad (3)$$

where $\langle \dots \rangle$ stands for the thermodynamical average, \mathcal{T} stands for the time-ordering operation, and $\hat{\psi}_{\mathcal{H}}(\mathbf{r}, t)$ denotes the field operator in the Heisenberg picture in the basis of the full Hamiltonian \mathcal{H} which contains kinetics, light-matter, and many-body interaction terms.

Using a standard quantum-field formalism, the effects of the many-body interaction can be conveniently cast in terms of the many-body self-energy $\hat{\Sigma}(1, 2)$. Using the Dyson recursive relation, the full field-dependent and interacting Green's function is given in terms of a field-dependent self-energy $\hat{\Sigma}$ and of a bare Green's function \hat{G}_0 as follows [25,26]:

$$\hat{G}(1, 1'; \mathbf{A}) = \hat{G}_0(1, 1'; \mathbf{A}) + \int_{\bar{2}, \bar{3}} \hat{G}_0(1, \bar{2}; \mathbf{A}) \hat{\Sigma}(\bar{2}, \bar{3}; \mathbf{A}) \hat{G}(\bar{3}, 1'; \mathbf{A}). \quad (4)$$

Equivalently, we have

$$\hat{G}^{-1}(1, 1'; \mathbf{A}) = \hat{G}_0^{-1}(1, 1'; \mathbf{A}) - \hat{\Sigma}(1, 1'; \mathbf{A}). \quad (5)$$

From now on we assume an external gauge field along the y axis, $\mathbf{A}(1) = A(1)\hat{y}$. The thermodynamical physical current, $\mathbf{J}(1; \mathbf{A}) = J(1; \mathbf{A})\hat{y}$, in Dirac systems can now be obtained as

$$J(1; \mathbf{A}) = -i \int_{1', 1''} \text{tr}[\hat{\Lambda}_1^{(0)}(1, 1'; 1'') \hat{G}(1, 1''; \mathbf{A})], \quad (6)$$



FIG. 1. Diagrammatic representation of the impurity self-energy in the self-consistent Born approximation. The solid line denotes the renormalized electronic Green's function, whereas the dashed lines connected by a cross represent the impurity scattering governed by the statistical correlations in Eq. (9).

where we denoted $1^+ \equiv (\mathbf{r}_1, t_1 + 0^+)$ and “tr” stands for the “trace” operation over all spinor indexes, i.e., $\text{tr}[\hat{A}\hat{B}] = \sum_{ss'} [A_{ss'} B_{s's}]$. The bare one-photon current vertex is hence obtained in terms of variational derivatives of the noninteracting Green's function versus the gauge field:

$$\begin{aligned} \hat{\Lambda}_1^{(0)}(1, 1'; 1'') &= \left. \frac{\delta \hat{G}_0^{-1}(1, 1'; \mathbf{A})}{\delta A(1'')} \right|_{\mathbf{A} \rightarrow \mathbf{0}} \\ &= -e v \hat{\sigma}_y \delta(1 - 1') \delta(1 - 1''). \end{aligned} \quad (7)$$

Because of the linear dispersion of the Dirac model, the two- and three-photon current vertices are of course null at the noninteracting level. However, as we are going to see, the presence of a field-dependent self-energy $\hat{\Sigma}(1, 1'; \mathbf{A})$ in Eq. (5) breaks the linear dependence of the inverse Green's function $\hat{G}^{-1}(1, 1'; \mathbf{A})$ on the external field, and it is expected to give rise to higher-order n -photon current vertices. More precisely, such nonlinear processes can be computed in terms of multipoint correlation functions for n -photon vertex operators:

$$\hat{\Lambda}_n(1', 1''; 1, \dots, n) = \frac{1}{(n-1)!} \left. \frac{\delta^n \hat{G}^{-1}(1', 1''; \mathbf{A})}{\delta A(1), \dots, \delta A(n)} \right|_{\mathbf{A} \rightarrow \mathbf{0}}. \quad (8)$$

The possibility of obtaining a computationally affordable expression for $\hat{\Lambda}_n(1', 1''; 1, \dots, n)$ depends of course on the specific characteristics of the scattering source.

In the following we focus on the role of elastic disorder or impurity scattering, which, along with a particularly simple structure allowing for a direct computation, preserves in Dirac materials the fundamental frequency dependence of the self-energy, which is a crucial ingredient in determining the nonlinear electromagnetic response.

One-particle impurity self-energy

We consider scattering on random local impurity centers with density n_{imp} and potential $V_{\text{imp}}(\mathbf{r}) = \sum_i V_i \delta(\mathbf{r} - \mathbf{R}_i)$, where \mathbf{R}_i are the coordinates of the lattice sites. We assume standard Born impurity correlations [27–29], so that $\langle V_{\text{imp}}(\mathbf{r}) \rangle = 0$ and the effective scattering potential reads

$$V(1, 2) = \langle V_{\text{imp}}(\mathbf{r}_1) V_{\text{imp}}(\mathbf{r}_2) \rangle_{\text{imp}} = n_{\text{imp}} V_{\text{imp}}^2 \delta(\mathbf{r}_1 - \mathbf{r}_2), \quad (9)$$

where the average $\langle \dots \rangle_{\text{imp}}$ is meant over all the random impurity configurations and where V_{imp} parametrizes the strength of impurity scattering. A diagrammatic representation of the self-energy is shown in Fig. 1, where the cross represents an impurity center and dashed lines represent the multiple scattering on each center, which in the Born scheme is assume

to happen no more than twice. Such a self-energy scheme is thus valid in the dilute limit and for small impurity scattering.

In the absence of external fields, the lowest-order self-consistent Born self-energy reads

$$\begin{aligned} \hat{\Sigma}(z) &= n_{\text{imp}} V_{\text{imp}}^2 \sum_{\mathbf{k}} \hat{G}(\mathbf{k}, z) \\ &= \gamma_{\text{imp}} S_{\text{cell}} \int \frac{d^2 k}{(2\pi)^2} \hat{G}(\mathbf{k}, z), \end{aligned} \quad (10)$$

where $\gamma_{\text{imp}} = n_{\text{imp}} V_{\text{imp}}^2$, S_{cell} is the two-dimensional unit-cell area, and the variable z lies in the complex frequency space. Due to the isotropic impurity scattering the self-energy spinor structure is trivial as $\hat{\Sigma}(z) = \Sigma(z) \hat{I}$, and therefore the Green's function can be explicitly written as follows:

$$\hat{G}(\mathbf{k}, z) = \frac{S(z) \hat{I} + \hbar v \hat{\sigma} \cdot \mathbf{k}}{S(z)^2 - (\hbar v k)^2}, \quad (11)$$

where $S(z) = z + \mu_0 - \Sigma(z)$.

The introduction of a high-energy (ultraviolet) cutoff is an unavoidable requirement of Dirac models. There is, however, a relatively large degree of freedom in the way in which it is introduced, and particular care is needed in order to avoid spurious results and to preserve physical consistencies, such as Ward identities, and gauge invariance. Dimensional regularization has proved to be a formidable tool to ensure that physical correctness is preserved [22,23]. We consider the evaluation of the disorder self-energy which displays a primary diverging integral. In arbitrary D dimensions, we have thus

$$\Sigma(z) = \frac{\gamma_{\text{imp}} N_{\text{cell}} S_{\text{cell}}^D}{(\hbar v)^D} \int \frac{d^D \ell}{(2\pi)^D} \frac{S(z)}{S(z)^2 - \ell^2}. \quad (12)$$

Note that the above integral in D dimensions can be solved in terms of Euler's gamma function $\Gamma_E(z)$ by utilizing the following identity [23]:

$$\int \frac{d^D \ell}{(2\pi)^D} \frac{1}{(\ell^2 + \Delta)^n} = \frac{1}{(4\pi)^{D/2}} \frac{\Gamma_E(n - \frac{D}{2})}{\Gamma_E(n)} \left(\frac{1}{\Delta} \right)^{n-D/2}. \quad (13)$$

We set $D = d - \epsilon$, where $d = 2$ is the physical dimension and $\epsilon \rightarrow 0$. Note that $\Gamma_E(\epsilon/2) \approx 2/\epsilon$ for $\epsilon \rightarrow 0$ and

$$\lim_{\epsilon \rightarrow 0} \frac{(X^2)^{-\epsilon/2}}{\epsilon/2} = \ln \left[\frac{W^2}{X^2} \right], \quad (14)$$

where W is a proper ultraviolet energy cutoff and where we use the prescription $\lim_{\epsilon \rightarrow 0} 1/\epsilon \equiv \ln[W]$. The above procedure of dimensional regularization is employed in a similar way in the evaluation of all the momentum integrals in this paper.

Eventually, we obtain the following self-consistent formula for the self-energy:

$$\Sigma(z) = -U S(z) \ln \left[-\frac{W^2}{S(z)^2} \right], \quad (15)$$

where U is a dimensionless parameter representing the electron-impurity scattering strength,

$$U = \frac{\gamma_{\text{imp}} S_{\text{cell}}}{4\pi (\hbar v)^2}. \quad (16)$$

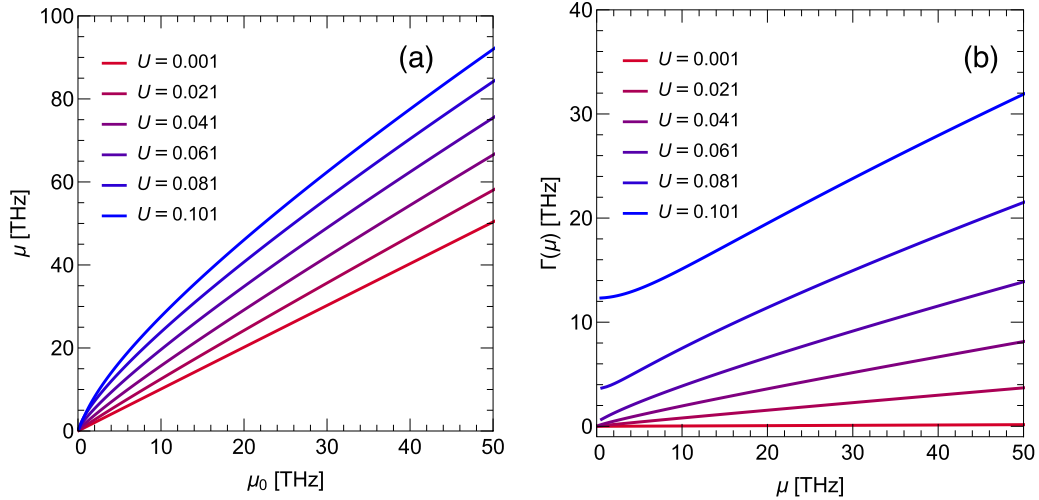


FIG. 2. (a) Renormalized chemical potential $\mu = \mu_0 - \text{Re}\Sigma(0)$ as a function of the bare chemical potential μ_0 . (b) Quasiparticle relaxation rate $\Gamma(\mu) = -\text{Im}\Sigma(0)$ vs μ . The crossover from the Boltzmann and the quantum regime is qualitatively signaled in this context by the departure from a linear behavior for both quantities.

In a direct comparison with graphene, we have $S_{\text{cell}} = \sqrt{3}a^2/2$ and $\hbar v = 3at_0/2$, where $a \approx 0.246$ nm is the lattice constant and $t_0 \sim 3$ eV is the nearest-neighbor hopping energy. In order to preserve the number of states, S_{cell} defines also an effective two-dimensional (2D) Brillouin zone, $V_{\text{BZ}} = 4\pi^2/S_{\text{cell}}$, which, employing the isotropic symmetry, defines a momentum cutoff k_c , $\pi k_c^2 = V_{\text{BZ}}$, and a natural ultraviolet energy cutoff $W = \hbar v k_c$ for the Dirac linear dispersion. Using the above parameters for graphene, we get $W = 7.2$ eV.

Numerical results of the self-energy at the Fermi level are shown in Fig. 2, where the renormalized chemical potential $\mu = \mu_0 - \text{Re}\Sigma(0)$ [Fig. 2(a)] conveys information about the real part of the self-energy and the relaxation rate $\Gamma(\mu) = -\text{Im}\Sigma(0)$ [Fig. 2(b)] governs the damping processes. It is worth remarking that for the impurity scattering the quasiparticle relaxation rate $\Gamma(\mu)$ does not vanish on the Fermi surface, in contrast with the standard Fermi-liquid paradigm.

III. MANY-BODY-DRIVEN MULTIPHOTON VERTEX GENERATION

The analytical expression of the functional dependence of the one-particle self-energy on the external field allows, within the spirit of a Kadanoff-Baym approach, the derivation of a closed set of self-consistent equations governing the transport properties at the chosen (linear or nonlinear) order. For Dirac materials, such as graphene, where the second-order response vanishes by symmetry, particular attention is paid to the *third-order* response and, within this framework, to the third harmonic generation. At the noninteracting level, vertex corrections are null, and the third harmonic generation is governed by the well-known “square” diagram with bare one-photon current vertices at the corners [4].

Things are much more complex in the presence of many-body interactions where the intrinsic dependence of the self-energy on the frequency and on external fields triggers nonlinear effects which are not predictable at the noninteracting level or within a phenomenological model using a constant

(frequency independent and external field independent) one-particle scattering rate.

A careful investigation of the many-body effects driven by disorder scattering, at the lowest-order self-consistent Born level, is remarkably enlightening since it preserves all the relevant nonlinearity but with a particularly simple expression for the self-energy which depends linearly on the fully interacting Green’s function in the presence of an external field:

$$\hat{\Sigma}(1, 2) = V(1, 2)\hat{G}(1, 2). \quad (17)$$

Here, $V(1, 2)$ stands for the many-body interaction potential, which, for the impurity-driven scattering, is given by Eq. (9).

It is worth stressing that such a simple linear relation as Eq. (9) between self-energy and the Green’s function holds true within a mean-field scheme for other kinds of scattering, e.g., electron-electron or electron-phonon. In this case the formal Kadanoff-Baym derivation and the diagrammatic theory that will be derived in the next sections remain still valid upon replacement of the appropriate interaction potential $V(1, 2)$, namely, $V(1, 2) \propto e^2\delta(t_1 - t_2)/|\mathbf{r}_1 - \mathbf{r}_2|$ for the Coulomb interaction and $V(\mathbf{q}, i\omega_m) \propto g_{\mathbf{q}}^2 D(\mathbf{q}, i\omega_m)$ for the electron-phonon interaction, where $g_{\mathbf{q}}$ is the electron-phonon coupling constant and $D(\mathbf{q}, i\omega_m) = -2\omega_{\mathbf{q}}/(\omega_m^2 + \omega_{\mathbf{q}}^2)$ is the retarded phonon propagator in the Matsubara frequency for a generic phonon mode with dispersion $\omega_{\mathbf{q}}$.

On this basis, after performing lengthy but straightforward algebra, we can construct a diagrammatic theory for the third-order response function of graphene as a two-dimensional Dirac material. Feynman diagrams for the third harmonic response function $\chi^{(3)}(1; 2, 3, 4)$ are depicted in Fig. 3. Here, solid lines represent Green’s functions, wavy lines represent the incoming or outgoing photons, and the empty and filled symbols represent the bare and renormalized n -photon vertices, respectively, where n can be identified by the number of attached wavy lines (photons).

A key role in this context is played by the multiphoton ($n > 1$) current vertices $\hat{\Lambda}_n(1', 1''; 1, \dots, n)$. A close inspection reveals that each fully dressed n -photon vertex

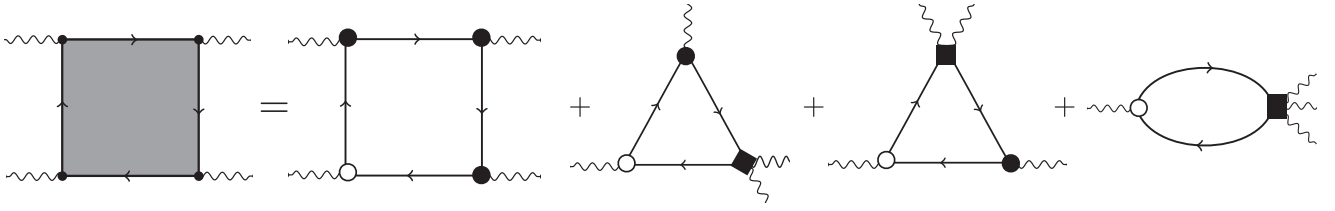


FIG. 3. Diagrams for the third-order response function of graphene as a two-dimensional Dirac material in terms of *renormalized* one-, two-, and three-photon vertices (where n is given by the number of attached wavy lines (photons)). The empty circle represents the one-photon current vertex at the noninteracting level [Eq. (7)], whereas filled symbols represent fully renormalized n -photon vertices.

$\hat{\Lambda}_n(1', 1''; 1, \dots, n)$ can be expressed in the self-consistent (Bethe-Salpeter-like) form (Fig. 4)

$$\begin{aligned} \hat{\Lambda}_n(1', 1''; 1, \dots, n) &= \hat{\lambda}_n(1', 1''; 1, \dots, n) \\ &+ \int_{\bar{2}, \bar{3}} \hat{K}_n(1', 1''; \bar{2}, \bar{3}) \hat{\Lambda}_n(\bar{2}, \bar{3}; 1, \dots, n), \end{aligned} \quad (18)$$

where the term $\hat{\lambda}_n(1', 1''; 1, \dots, n)$ (empty symbols in Fig. 4) can be expressed in terms of *lower-order* multiphoton vertices (see Fig. 5). It should be noticed that, while $\hat{\lambda}_1(1', 1''; 1)$ reduces to the bare one-photon vertex $\hat{\lambda}_1(1', 1''; 1) = \hat{\lambda}_1^{(0)}(1', 1''; 1) = -ev\hat{\sigma}_y\delta(1-1')\delta(1-1'')$ in the noninteracting limit $U \rightarrow 0$, the two- and three-photon vertex terms $\hat{\lambda}_2(1', 1''; 1, \dots, n)$, $\hat{\lambda}_3(1', 1''; 1, \dots, n)$ and so the fully dressed multiphoton vertices $\hat{\Lambda}_2(1', 1''; 1, \dots, n)$, $\hat{\Lambda}_3(1', 1''; 1, \dots, n)$ are triggered by the many-body impurity scattering. By using the symmetry enforced by isotropic impurity scattering, one can see that each n -photon vertex has a specific Pauli structure. This property can be employed to define a scalar vertex function for each n -photon vertex, namely, $\hat{\Lambda}_n = (-ev\hat{\sigma}_y)^n \Lambda_n$ and $\hat{\lambda}_n = (-ev\hat{\sigma}_y)^n \lambda_n$. With this notation in the noninteracting case we have $\Lambda_1^{(0)} = \lambda_1^{(0)} = 1$ and $\Lambda_{n>1}^{(0)} = \lambda_{n>1}^{(0)} = 0$.

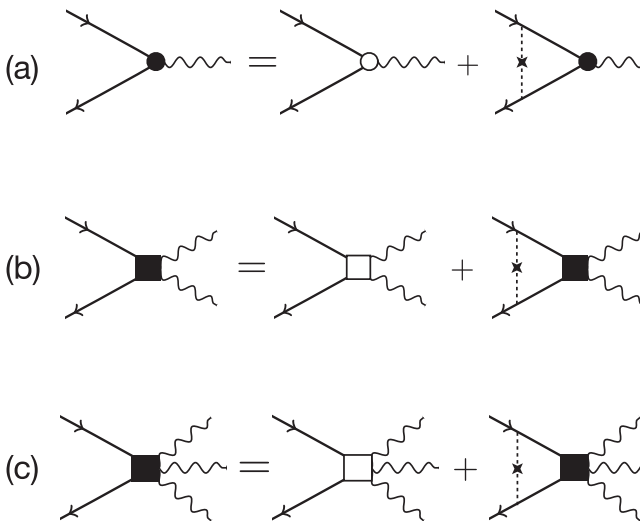


FIG. 4. Diagrams for the self-consistent Bethe-Salpeter renormalization of n -photon vertex functions Λ_n , where (a), (b), and (c) correspond to $n = 1$, $n = 2$, and $n = 3$, respectively.

IV. MANY-BODY DRESSED THIRD HARMONIC GENERATION

The diagrammatic expressions in Figs. 3–5 are valid for any generic third-order optical response. A particularly interesting case is the third harmonic generation (THG), which, using the translational invariance symmetry and in the Matsubara space, can be conveniently written as

$$\chi_{\text{THG}}^{(3)}(m) = \frac{1}{\beta} \sum_n P(n, n+m, n+2m, n+3m). \quad (19)$$

Here, $m = i\omega_m$ represents the photon bosonic energy, and $n = i\omega_n$ is the internal fermionic energy to be summed over.

The corresponding third harmonic optical conductivity $\sigma_{\text{THG}}^{(3)}(\omega)$ can be hence obtained after analytical continuation $i\omega_m \rightarrow \hbar\omega + i0^+$ as

$$\sigma_{\text{THG}}^{(3)}(\omega) = i \frac{\chi_{\text{THG}}^{(3)}(\omega)}{\omega^3}. \quad (20)$$

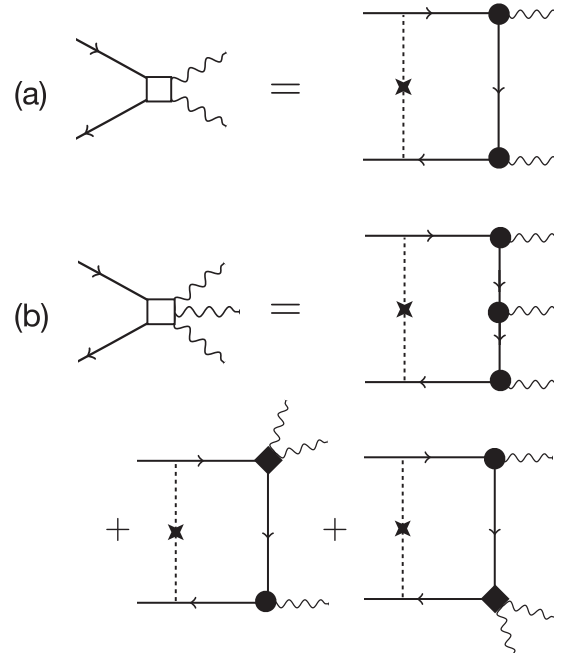


FIG. 5. Diagrams for the interaction-induced two- and three-photon vertices $\lambda_{n=2,3}$ are given in (a) and (b), respectively.

After straightforward algebra, one can thus obtain [18]

$$\begin{aligned} \chi_{\text{THG}}^{(3)}(\omega) = & \int_{-\infty}^{+\infty} \frac{d\epsilon}{2\pi i} \{n_{\text{F}}(\epsilon)P^{\text{RRRR}} - n_{\text{F}}(\epsilon + 3\hbar\omega)P^{\text{AAAA}} \\ & + [n_{\text{F}}(\epsilon + \hbar\omega) - n_{\text{F}}(\epsilon)]P^{\text{ARRR}} \\ & + [n_{\text{F}}(\epsilon + 2\hbar\omega) - n_{\text{F}}(\epsilon + \hbar\omega)]P^{\text{AARR}} \\ & + [n_{\text{F}}(\epsilon + 3\hbar\omega) - n_{\text{F}}(\epsilon + 2\hbar\omega)]P^{\text{AAAR}}\}, \end{aligned} \quad (21)$$

where $n_{\text{F}}(\epsilon) = 1/[\exp(\epsilon/T) + 1]$ is the Fermi-Dirac factor with temperature T in units of $1/k_{\text{B}}$, with k_{B} being the Boltzmann constant.

For the sake of compactness, we use here a short notation where $P^{\nu_0\nu_1\nu_2\nu_3} = P(\epsilon_0, \nu_0, \epsilon_1, \nu_1, \epsilon_2, \nu_2, \epsilon_3, \nu_3)$, where $\epsilon_j, \nu_j = \epsilon + j\omega + j\eta_{\nu_j}$ ($j = 0, 1, 2, 3$) and where η_{ν_j} is a vanishingly small quantity with $\eta_{\nu_j} > 0$ if $\nu_j = \text{R}$ and $\eta_{\nu_j} < 0$ if $\nu_j = \text{A}$. Notice also that $P^{\text{AAAA}} = (P^{\text{RRRR}})^*$.

As depicted in Fig. 3, the P function contains four different contributions, $P = P_1 + P_2 + P_3 + P_4$, associated with square (P_1), triangle (P_2 and P_3), and bubble (P_4) diagrams, respectively. More explicitly, we can write

$$\begin{aligned} P_1(z_0, z_1, z_2, z_3) = & \alpha Q_1(z_0, z_1)Q_1(z_1, z_2)Q_1(z_2, z_3) \\ & \times \Omega_1(z_0, z_1, z_2, z_3), \end{aligned} \quad (22)$$

where $\alpha = e^4 v^2 N_f / 2\pi \hbar^2$. The sum over spin and valley indices just leads to an overall degeneracy factor $N_f = N_s N_v$, where $N_s = 2$ and $N_v = 2$. The function $\Omega_1(z_0, z_1, z_2, z_3)$ represents the square diagram neglecting vertex renormalization,

$$\begin{aligned} \Omega_1(z_0, z_1, z_2, z_3) = & \frac{\gamma_{\text{imp}}}{2U} \sum_{\mathbf{k}} \text{Tr}[\hat{\sigma}_y \hat{G}(\mathbf{k}, z_0) \hat{\sigma}_y \hat{G}(\mathbf{k}, z_1) \hat{\sigma}_y \\ & \times \hat{G}(\mathbf{k}, z_2) \hat{\sigma}_y \hat{G}(\mathbf{k}, z_3)], \end{aligned} \quad (23)$$

and $Q_1(z_i, z_j) = \Lambda_1(z_i, z_j)/\lambda_1(z_i, z_j)$, where as defined above, $\lambda_1(z_i, z_j) = 1$. $Q_1(z_i, z_j)$ thus represents the one-photon Bethe-Salpeter renormalization factor, which is discussed in detail in Appendix A. In a similar way we can write the contributions of the two triangle diagrams as

$$\begin{aligned} P_2(z_0, z_1, z_2, z_3) = & \alpha Q_1(z_2, z_3)Q_2(z_0, z_2)\lambda_2(z_0, z_1, z_2) \\ & \times \Omega_2(z_0, z_2, z_3), \end{aligned} \quad (24)$$

where $\lambda_2(z_0, z_1, z_2)$ is the lowest-order two-photon current vertex [Fig. 5(a)],

$$\Omega_2(z_0, z_2, z_3) = -\frac{\gamma_{\text{imp}}}{2U} \sum_{\mathbf{k}} \text{Tr}[\hat{\sigma}_y \hat{G}(\mathbf{k}, z_0) \hat{G}(\mathbf{k}, z_2) \hat{\sigma}_y \hat{G}(\mathbf{k}, z_3)], \quad (25)$$

and $Q_2(z_i, z_j) = \Lambda_2(z_i, z_k, z_j)/\lambda_2(z_i, z_k, z_j)$ is the two-photon Bethe-Salpeter renormalization factor (see Appendix B). Furthermore, we can also express the triangle diagram as

$$\begin{aligned} P_3(z_0, z_1, z_2, z_3) = & \alpha Q_1(z_0, z_1)Q_2(z_1, z_3)\lambda_2(z_1, z_2, z_3) \\ & \times \Omega_3(z_0, z_1, z_3), \end{aligned} \quad (26)$$

where

$$\Omega_3(z_0, z_1, z_3) = -\frac{\gamma_{\text{imp}}}{2U} \sum_{\mathbf{k}} \text{Tr}[\hat{\sigma}_y \hat{G}(\mathbf{k}, z_0) \hat{\sigma}_y \hat{G}(\mathbf{k}, z_1) \hat{G}(\mathbf{k}, z_3)]. \quad (27)$$

Finally, we can express the bubble term as

$$\begin{aligned} P_4(z_0, z_1, z_2, z_3) = & \alpha \lambda_3(z_0, z_1, z_2, z_3) Q_3(z_0, z_3) \\ & \times X_1(z_0, z_3), \end{aligned} \quad (28)$$

where $Q_3(z_i, z_k, z_l, z_j) = \Lambda_3(z_i, z_j)/\lambda_3(z_i, z_k, z_l, z_j)$ is the three-photon Bethe-Salpeter renormalization factor (see Appendix C), with $\lambda_3(z_0, z_1, z_2, z_3)$ being the lowest-order three-photon vertex function [Fig. 5(b)], and

$$X_1(z, z') = \frac{\gamma_{\text{imp}}}{2U} \sum_{\mathbf{k}} \text{Tr}[\hat{\sigma}_y \hat{G}(\mathbf{k}, z) \hat{\sigma}_y \hat{G}(\mathbf{k}, z')]. \quad (29)$$

A close inspection of the topological structure of the diagrams for the three-photon vertex [see Fig. 5(b) and Appendix C] permits further simplifications as

$$\begin{aligned} P_4(z_0, z_1, z_2, z_3) = & U Q_3(z_0, z_3) X_1(z_0, z_3) \\ & \times \sum_{i=1}^3 P_i(z_0, z_1, z_2, z_3). \end{aligned} \quad (30)$$

Using $Q_3 = Q_1 = 1/[1 - UX_1]$ (see Appendix C), we find the following result for the total P function:

$$P(z_0, z_1, z_2, z_3) = Q_3(z_0, z_3) \sum_{i=1}^3 P_i(z_0, z_1, z_2, z_3). \quad (31)$$

We can thus see that the net impact of the three-photon vertex diagram in the third-order response function simply leads to the appearance of the three-photon renormalization factor $Q_3(z_0, z_3)$ on the contribution of the other diagrams. The explicit expressions of λ_n , Q_n , and Ω_n are provided in great detail in Appendixes A–C for the one-, two-, and three-photon vertex Bethe-Salpeter renormalizations.

Equipped with all the analytical expressions needed for the computation of the optical properties of the third harmonic generation response, in the following section we present numerical results for the low-energy intraband third harmonic conductivity of a two-dimensional Dirac modeling of graphene.

V. RESULTS AND DISCUSSION

Based on a mere dimensional analysis, we can conveniently express the zero-temperature third harmonic conductivity of graphene in terms of a dimensionless function $f_3(x, y, z)$:

$$\sigma_{\text{THG}}^{(3)}(\omega) = \frac{\sigma_0}{E_0^2} \left(\frac{t_0}{\hbar\omega}\right)^4 f_3\left(\frac{\hbar\omega}{\mu_0}, \frac{\mu}{\Gamma}, U\right), \quad (32)$$

where $\mu = \mu_0 - \text{Re}\Sigma(0)$ is the renormalized chemical potential, $\Gamma = \Gamma(0) = -\text{Im}\Sigma(0)$ is the Fermi surface scattering rate, $\sigma_0 = e^2/4\hbar$ is the universal conductivity including the spin and valley degeneracy, and $E_0 = \pi t_0/\sqrt{3}ea \approx 22.0$ V/nm is a characteristic electric-field scale determined by the interatomic hopping energy t_0 and by the lattice constant a . In the dc limit $\omega \rightarrow 0$, $\lim_{x \rightarrow 0} f_3(x, y, z)$, we recover the transport regime discussed in Ref. [18]. The appearance of the bare chemical potential μ_0 in the definition of x , and of the renormalized one, μ , in the definition of y , is dictated by the different roles of μ_0 and μ in governing

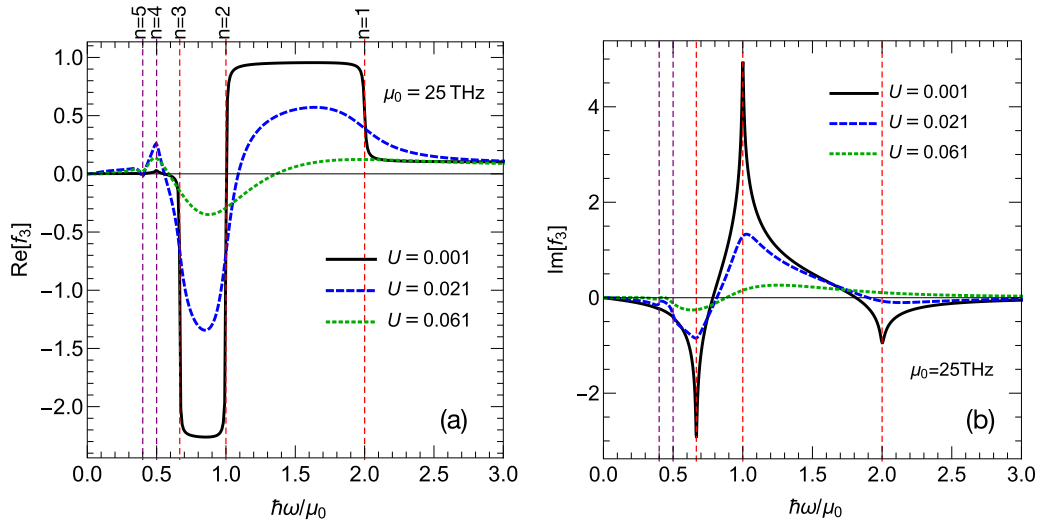


FIG. 6. (a) Real and (b) imaginary parts of the THG conductivity for the whole range of intraband to interband regimes. The vertical red dashed lines indicate the location of the n -photon interband resonance as $\hbar\omega = 2\mu_0/n$ with $n = 1, 2, 3$, whereas the vertical purple dashed lines reveal the frequencies of four- and five-photon incoherent transitions with $n = 4, 5$. Note that the purely intraband features for $\omega \rightarrow 0$, although present, are not visible on this scale in the f_3 function.

the dc and optical properties, as discussed in more detail below.

Besides the obvious role of the real part of the third harmonic generation, the imaginary part of the conductivity bears also a strong relevance. As a matter of fact, the THG efficiency η_{THG} scales indeed as $\eta_{\text{THG}} = I_{\text{THG}}/I_{\text{in}} \propto I_{\text{in}}^2 |\sigma_{\text{THG}}^{(3)}|^2$, where I_{in} and I_{THG} stand for the incident and THG intensities, respectively. For computational reasons it is convenient to directly calculate, using Eqs. (20) and (21), the real part of the nonlinear conductivity $\text{Re}[\sigma_{\text{THG}}^{(3)}]$, or equivalently, $\text{Re}[f_3] \propto \omega \text{Im}[\chi_{\text{THG}}^{(3)}]$. The imaginary part, $\text{Im}[\sigma_{\text{THG}}^{(3)}]$ (or $\text{Im}[f_3] \sim \omega \text{Re}[\chi_{\text{THG}}^{(3)}]$), can thus be obtained by means of the Kramers-Kronig relations:

$$\text{Re}[\chi_{\text{THG}}^{(3)}(\omega)] = \frac{2}{\pi} \int_0^\infty d\omega' \frac{\omega' \text{Im}[\chi_{\text{THG}}^{(3)}(\omega')]}{\omega^2 - \omega'^2}. \quad (33)$$

In the high-frequency regime, the third harmonic generation response function $\chi_{\text{THG}}^{(3)}(\omega)$ is described by *purely interband* transitions, $\chi_{\text{THG,inter}}^{(3)}(\omega)$, giving rise to steplike functions at $\hbar\omega \approx 2\mu_0/n$ corresponding to $n = 1, 2, 3$ photon resonances, where the three-photon resonance at $\hbar\omega \approx 2\mu_0/3$ defines the interband optical edge. The low frequency $\hbar\omega \ll \mu$ corresponds to the *purely intraband* regime of third harmonic optical conductivity, which will be discussed in Sec. VB. In addition to this structure, in the intermediate frequency range, we reveal incoherent four- and five-photon transitions with *mixed intra- and interband* characters. These features will be the focus of Sec. VA.

A. Four- and five-photon incoherent transitions

The full quantum treatment of many-body interaction with Green's functions and Kubo formalism predicts intriguing spectral features. In Figs. 6(a) and 6(b) we plot the real and imaginary parts of the THG function $f_3 \sim \omega^4 \sigma_{\text{THG}}^{(3)}$ versus the laser frequency ω in the whole intra-

band to interband frequency range for different values of the scattering strength U . In the almost clean limit ($U = 0.001$) the dominant features are the multiphoton interband resonances at $\hbar\omega \approx 2\mu_0/n$ with $n = 1, 2, 3$, which appear as smeared structures by the interaction in the real and imaginary parts. Note that on this scale the purely intraband features are not visible since their magnitude scales as ω^4 . Upon increasing the scattering strength, besides the obvious smearing of the interband features, we notice the appearance of resonances below the interband edge $\hbar\omega \approx 2\mu_0/3$, i.e., in the intraband range. A closer look reveals that such spectral features occur at frequencies $\hbar\omega = 2\mu_0/n$ with $n = 4, 5$ (purple vertical dashed lines in Fig. 6), namely, at energies corresponding to four- and five-photon resonances, respectively.

The very possibility of observing four- and five-photon transitions in the third-order conductivity is quite surprising, and it calls for further and deeper investigation. Also worth noticing is the fact that although a full many-body treatment is here enforced, the n -photon resonances ($n = 1, \dots, 5$) occur at the energies $\hbar\omega \approx 2\mu_0/n$ dictated by the *bare* chemical potential μ_0 , rather than by the effective renormalized one, μ . This puzzling result has not been detected previously in the literature since in noninteracting models as well as in phenomenological models where only a constant scattering rate Γ (the imaginary part of the self-energy) is included, no renormalization of the chemical potential is operative, and $\mu = \mu_0$.

The appearance of four- and five-photon transitions in the third-order conductivity can be rationalized by considering at the simplest level the square diagrams depicted in Fig. 3 furthermore neglecting the Bethe-Salpeter vertex renormalization. In this case, according to Eq. (22), the kernel response function P in Eq. (21) will read simply $P(z_0, z_1, z_2, z_3) = P_1(z_0, z_1, z_2, z_3) \propto \Omega_1(z_0, z_1, z_2, z_3)$. The explicit expression of $\Omega_1(z_0, z_1, z_2, z_3)$ is long and cumbersome, and it is provided in Appendix C. The main feature in regard to the present issue

TABLE I. Predicted n -photon transitions $\hbar\omega = 2\mu_0/n$ in the third-order optical conductivity. The transitions marked with an asterisk are expected to have null spectral weight for the elastic scattering considered here, but they might gain a finite spectral weight in the presence of inelastic scattering (see discussion in the text).

Channel	ϵ range at $T = 0$	n -photon transition
RRRR	$-3\hbar\omega \leq \epsilon \leq 0$	$n = 1, 2, 3, 4, 5$
ARRR	$-\hbar\omega \leq \epsilon \leq 0$	$n = 1^*$
AARR	$-2\hbar\omega \leq \epsilon \leq -\hbar\omega$	$n = 1, 2^*, 3$
AAAR	$-3\hbar\omega \leq \epsilon \leq -2\hbar\omega$	$n = 1, 2, 3, 4, 5$

is that it depends as

$$\Omega_1(z_0, z_1, z_2, z_3) \propto \prod_{i \neq j=0, \dots, 3} \frac{1}{S(z_i) + S(z_j)}. \quad (34)$$

According to Eq. (34), multiphoton transitions can occur when $\text{Re}[S(z_i) + S(z_j)] = 0$ with $z_j = \epsilon + j\hbar\omega$. Neglecting for the moment the contribution of the self-energy, this implies that $\epsilon = -\mu_0 - (i + j)\hbar\omega/2$. We assume for simplicity $\mu >$

0 and $T = 0$, and we focus on the RRRR channel. Enforcing the boundary conditions $-3\hbar\omega \leq \epsilon \leq 0$ which originate from the factor $n_F(\epsilon) - n_F(\epsilon + 3\omega)$ in Eq. (21), we get that possible n -photon interband transitions can occur at $\hbar\omega = 2\mu_0/n$ with $n = 6 - (i + j)$, and considering $i, j = 0, 1, 2, 3$ with $i \neq j$, we obtain the possible values $n = 1, 2, 3, 4, 5$. A similar analysis can be applied to other channels where the possibility of detecting an n -photon transition is dictated by the integration window over ϵ [see the Fermi function prefactors in Eq. (21) for different channels] and by the retarded or advanced character of the complex frequencies z_i involved in the transition. More explicitly, it can be shown that n -photon transitions in each channel have a finite spectral weight only when z_i and z_j have the *same* (retarded or advanced) character, in a similar way as occurs in the linear optical response. With such a road map, we can analyze theoretically the possible appearance of multiphoton transitions in each separate contribution P^{RRRR} , P^{ARRR} , P^{AARR} , and P^{AAAR} . Our theoretical predictions are summarized in Table I, and the numerical results are shown in Figs. 7(a) and 7(b), in excellent agreement with each other.

The total nonlinear response is determined by the sum of *all* the channels. As we can see in Fig. 7(a), both RRRR and

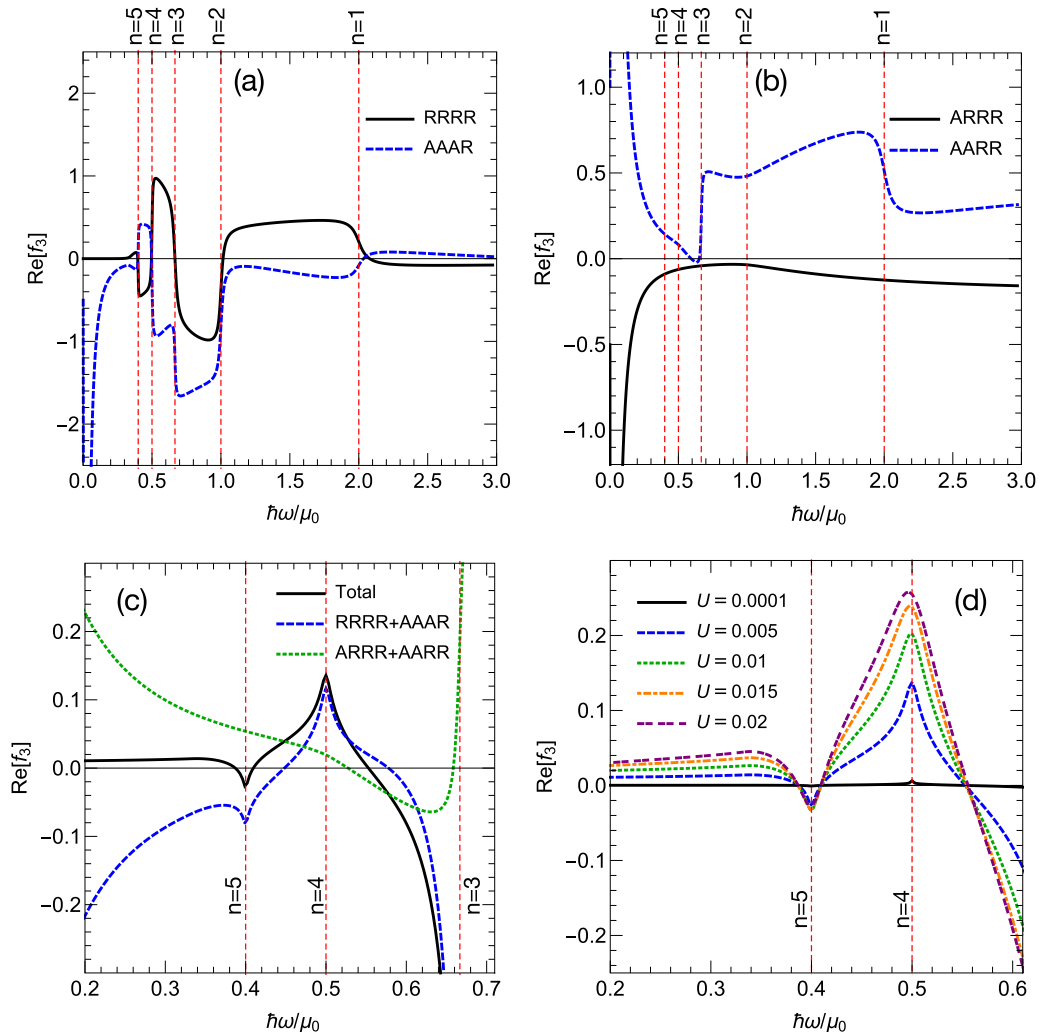


FIG. 7. (a)–(c) Different channel contributions (RRRR, AAAR, ARRR, and AARR) to the real part of the f_3 function for $U = 0.005$. (d) Evolution of the real part of the total f_3 function for different values of U . We set $\mu_0 = 25$ THz.

AAAR channels show steplike transitions at the four- and five-photon resonances, i.e., at $\hbar\omega \approx \mu_0/2$ and $\hbar\omega \approx 2\mu_0/5$, but with opposite sign. The sum of these two contributions would exactly cancel out in the clean limit $U = 0$. Such cancellation is, however, just partial for finite U (or finite Γ), leaving finite spectral structures at $\hbar\omega \approx \mu_0/2$ and $\hbar\omega \approx 2\mu_0/5$, as seen in Fig. 7(c). The behavior as a function of the scattering strength is shown in Fig. 7(d). As mentioned above, in the clean limit $U \rightarrow 0$ the multiphoton resonances at $n = 4, 5$ in the individual channels P^{RRRR} , P^{ARRR} , P^{AARR} , and P^{AAAA} cancel out exactly, and they are thus absent in the total response. However, such cancellation is not perfect in the presence of a finite electron-impurity scattering, leaving residual spectral structures at frequencies corresponding to the four- and five-photon resonances. The spectral weight of these multiphoton structures scales with the impurity scattering itself. The absence of four- and five-photon transitions in the clean (noninteracting) limit thus reveals that these transitions are in fact *incoherent transitions* with mixed inter- and intraband characters. The partial intraband character is highlighted by the transition weight being proportional to the relaxation rate Γ , whereas the partial interband character of such features is pointed out by their lying at finite frequency, i.e., at exactly the four- and five-photon resonance energy with the peak positions not affected by U . It is worth emphasizing that these incoherent transitions at finite frequency pinned by μ_0 are a peculiar property of nonlinear optical conductivity and they do not emerge in linear optical conductivity.

Now, we focus on the role of the many-body self-energy renormalization in determining the spectral features of the optical third harmonic generation response. As discussed above, n -photon transitions can be theoretically identified by enforcing the condition $\text{Re}[S(z_i) + S(z_j)] = 0$ together with $\epsilon = \epsilon_{\min}, \epsilon_{\max}$, where $\epsilon_{\min}, \epsilon_{\max}$ are the lower and upper energy integration limits for each channel. With such a prescription, neglecting the many-body self-energy, the n -photon transitions occur at $\hbar\omega \approx 2\mu_0/n$, where μ_0 is the bare chemical potential. It is, however, straightforward to check that the same holds true also in the presence of (frequency dependent) elastic scattering driven by disorder or impurity preserving the mirror symmetry with respect to the Dirac point. The analysis of linear optical conductivity is enlightening on this point. In a similar way to that in the third-order response function, at $T = 0$ the edge of the interband optical transitions is determined by the conditions $\text{Re}[S(\epsilon) + S(\epsilon + \hbar\omega)] = 0$ and $\text{Re}[S(\epsilon) + S^*(\epsilon + \hbar\omega)] = 0$, respectively, together with the constraints $\epsilon = 0, \epsilon = -\hbar\omega$ determined by the window of energy integration over ϵ . We thus obtain that the edge of optical interband transitions is determined by

$$\hbar\omega = 2\mu_0 - \text{Re}\Sigma(0) - \text{Re}\Sigma(-2\mu_0), \quad (35)$$

with a spectral weight I_{sw} that scales as

$$I_{\text{sw}} = |\text{Im}\Sigma^\nu(0) - \text{Im}\Sigma^{\nu'}(-2\mu_0)|, \quad (36)$$

where $\nu, \nu' = \text{A, R}$. The elastic impurity scattering self-energy respects the following symmetry relation owing to

symmetry of Dirac dispersion:

$$\text{Re}\Sigma(-\mu_0 - \epsilon) = -\text{Re}\Sigma(-\mu_0 + \epsilon), \quad (37)$$

$$\text{Im}\Sigma^{\text{R/A}}(-\mu_0 - \epsilon) = \text{Im}\Sigma^{\text{R/A}}(-\mu_0 + \epsilon), \quad (38)$$

$$\text{Im}\Sigma^{\text{A/R}}(-\mu_0 - \epsilon) = -\text{Im}\Sigma^{\text{A/R}}(-\mu_0 + \epsilon). \quad (39)$$

These relations imply in a direct way that (i) the interband optical edge in the linear optical conductivity is determined only by μ_0 and not by the renormalized chemical potential μ and (ii) only the retarded-retarded channel is responsible for the $n = 1$ photon transition thus observed in linear optics. Similar argumentations hold true in a straightforward way in nonlinear optics, where we conclude that (i) the n -photon transitions are determined only by μ_0 and not by the renormalized chemical potential μ and (ii) only retarded-retarded or advanced-advanced transitions show a sizable spectral weight and can thus be observed in the optical features.

The strict validity of these symmetry relations is affected in the presence of inelastic scattering where the even or odd symmetries with respect to the Dirac points are lifted. Considering, however, the realistic case of low-energy inelastic scattering (e.g., phonons), the breaking of the symmetry relations in the imaginary part in Eqs. (38) and (39) is limited to a narrow shell around the Fermi level, thus affecting only the $\hbar\omega \approx 2\mu_0$ resonance ($n = 1$). Inelastic scattering might thus reduce a bit the spectral weight of $n = 1$ photon transitions in the RRRR, AARR, and AAAR channels, and it might induce a finite spectral weight in the ARRR channel, which is predicted to be null under the above symmetry conditions valid, however, only for elastic scattering. Inelastic scattering would affect as well the symmetry relation for the real part of the self-energy, as it can be obtained by Kramers-Kronig transform of the imaginary part of the self-energy. Since the imaginary part of the self-energy is typically affected only in a narrow region around the Fermi level, we expect deviations from the symmetry relation in the real part in Eq. (37) to be relatively small and scaling with the strength of the inelastic coupling. Multiphoton transitions might be just slightly shifted from the edge determined by μ_0 .

B. Intraband THG conductivity

The analysis of the THG optical conductivity allows us to investigate in detail also the low-energy spectral features associated with the pure intraband processes, which are not easily visible in the dimensionless function f_3 . A phenomenological model previously obtained [2,3] based on density-matrix formalism and using a constant scattering rate is commonly used to describe qualitatively the low-frequency profile of THG conductivity in the Boltzmann regime where $\mu \gg \Gamma, \hbar\omega$:

$$\sigma_{\text{THG},\Gamma}^{(3)} = i \frac{C}{\mu(\hbar\omega + i\Gamma)^3}, \quad (40)$$

where $C > 0$ is a constant and Γ stands for a constant (frequency independent) scattering rate. A sketch of Eq. (40) is shown in Fig. 8(a). Equation (40) captures a similar physics to that of the Drude term in the linear optics. Indeed, in a similar way to that used to obtain the Drude term, such a purely intraband term can be obtained, in this phenomenolog-

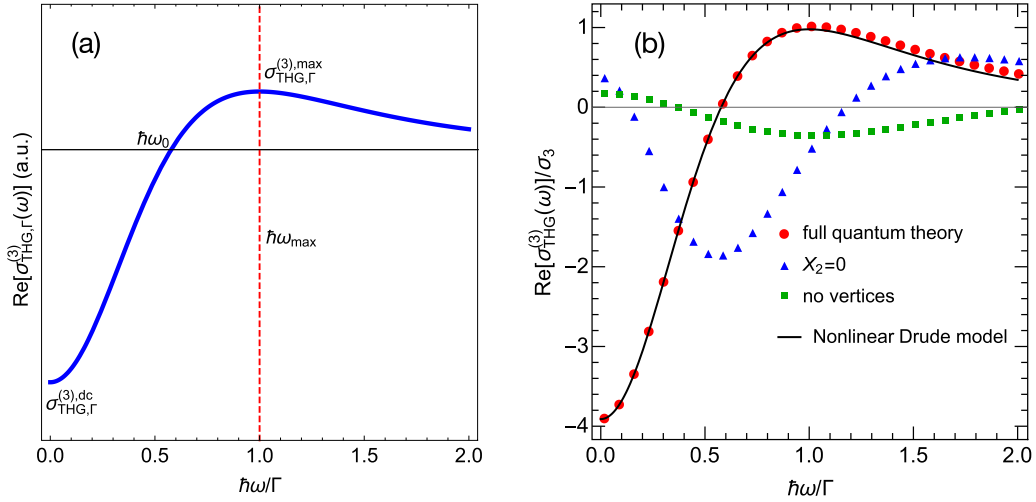


FIG. 8. (a) Spectral behavior of the purely intraband part of THG conductivity according to the phenomenological model of Eq. (40). The characteristic parameters defined in Eqs. (41)–(44) are here represented. (b) Real part of the intraband THG conductivity for $U = 0.013$ and $\mu_0 = 25$ THz computed at different levels of approximation and compared with the phenomenological model of Eq. (40). Red circles represent results for the full quantum theory including all diagrams in a conserving way, blue triangles correspond to a nonconserving analysis where the two-photon vertex renormalization is neglected by setting $X_2 = 0$, and green squares represent a further (nonconserving) approximation where *all* vertex renormalization processes are neglected. The solid line represents the phenomenological model of Eq. (40) with a fitting parameter $\Gamma \approx 0.017\mu_0$. Note that $\sigma_3 = 10^{11}\sigma_0^{(3)}$ with $\sigma_0^{(3)} = \sigma_0/E_0^2$.

ical framework, by replacing in the noninteracting model the frequency ω with the complex frequency $\omega \rightarrow \omega + i\Gamma$. Furthermore, like the Drude term in the linear response and unlike the interband counterpart ruled by μ_0 , the spectral properties of Eq. (40) are governed only by a couple parameters, namely, the renormalized chemical potential μ (ruling the magnitude of the intraband feature) and the relaxation rate Γ (ruling the energy scale of such intraband features). In more detail, the above model predicts, for any strength of Γ , a negative dc conductivity in the limit $\omega \rightarrow 0$,

$$\sigma_{\text{THG},\Gamma}^{(3),\text{dc}} = -\frac{C}{\mu\Gamma^3}, \quad (41)$$

as well as a maximum

$$\sigma_{\text{THG},\Gamma}^{(3),\text{max}} = \frac{C}{4\mu\Gamma^3}, \quad (42)$$

at

$$\hbar\omega_{\text{max}} = \Gamma, \quad (43)$$

and a zero $\sigma_{\text{THG},\Gamma}^{(3)}(\omega = \omega_0) = 0$ at

$$\hbar\omega_0 = \Gamma/\sqrt{3}. \quad (44)$$

See Fig. 8(a) for a graphical representation of the parameters defined above. Interestingly, the nonlinear Drude term scales inversely with the chemical potential, while the linear Drude conductivity is directly proportional to μ . This implies that nonlinear correction is more pronounced at a lower doping rate.

We are now in a position to compare the results of our quantum analysis, which includes in a conserving way many-body processes, with the phenomenological model of Eq. (40), where many-body effects are neglected. In Fig. 8(b) we compare such a phenomenological model (solid line) with the full quantum theory (red circles) for $U = 0.013$ and $\mu_0 =$

25 THz, showing a remarkable agreement. Such agreement is even more striking upon noticing that many-body effects (not present in the phenomenological model), i.e., the two-photon vertex renormalization, are widely ruling these intraband features. This can also be seen in Fig. 8(b), where we plot also the numerical results obtained by neglecting the two-photon vertex renormalization (blue triangles). The spectral profile in this case is quite different, showing, in particular, a positive value in the dc $\omega \rightarrow 0$. A further different result is obtained when *all* the vertex renormalizations are neglected (green squares).

Such agreement between the full quantum theory and the phenomenological model appears to be not accidental since it can be assessed in a numerically controlled way using Eq. (40) as a template. More precisely, we numerically determine in the full quantum theory, as a function of the scattering strength U , the dc limit $\sigma_{\text{THG}}^{(3),\text{dc}} = \sigma_{\text{THG}}^{(3)}(\omega = 0)$; the frequency ω_0 where the THG has the first low-frequency zero; the frequency ω_{max} where the THG conductivity has its first maximum; and the value $\sigma_{\text{THG}}^{(3),\text{max}}$ of the THG conductivity at $\omega = \omega_{\text{max}}$. As discussed above, in the phenomenological model all these parameters are not independent, but they obey the scaling relations described in Eqs. (41)–(44).

In Figs. 9(a)–9(d) we can thus compare for $\mu_0 = 25$ THz the mutual dependence of such characteristic spectral parameters as obtained from the numerical results of the many-body quantum theory and as estimated from the model in Eq. (40). We find an excellent agreement in the very weak scattering regime $U \rightarrow 0$ ($\Gamma \ll \mu$), with a noticeable departure for larger Γ . The nature of such deviation will be discussed later.

The striking resemblance for the pure intraband spectral features between the results of the conserving Kadanoff-Baym theory and the phenomenological model with a constant impurity scattering rate is somehow puzzling, and it prompts thus the fundamental question, How is possible that the full

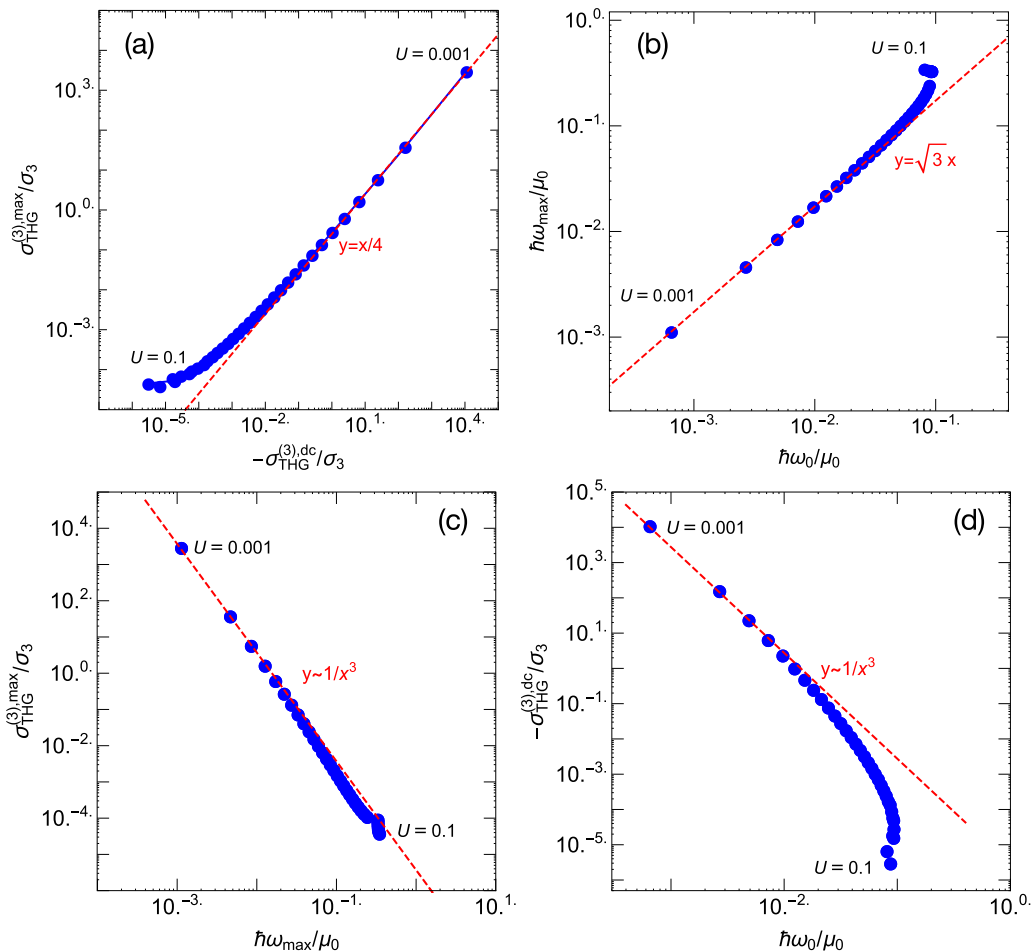


FIG. 9. Comparison between the full many-body theory and the phenomenological model given in Eq. (40). (a) Log-log scale plot of the maximum value of the real part of the intraband THG conductivity vs the third-order dc conductivity compared with linear scaling (dashed red line) obtained from the phenomenological formula. (b) Log-log scale plot of ω_{max} vs ω_0 , which is compared with a linear scaling line (dashed red line) based on the phenomenological model. (c) Cubic scaling of the maximum value of the real part of the intraband THG vs ω_{max} , which is valid only for small values of U . (d) Cubic scaling for third-order dc conductivity vs ω_0 , which is valid only for small values of U . Here, $\mu_0 = 25$ THz and $\sigma_3 = 10^{10}\sigma_0^{(3)}$ with $\sigma_0^{(3)} = \sigma_0/E_0^2$.

quantum theory, which contains crucial complex many-body effects, is *so remarkably similar* to a strongly approximate modeling where multiple scattering processes and many-body effects are essentially neglected? In this regard it is worth stressing that the constant- Γ model is itself a *conserving* approximation, where to a field-independent and frequency-independent self-energy correspond unrenormalized vertices. We rationalize thus the agreement between the constant- Γ model and the fully many-body theory on the basis of the requirement of a conserving analysis. This understanding prompts hence the crucial warning in the field: A reliable description at a microscopic level of the scattering processes unavoidably requires that they be addressed within a self-consistent conserving approach, whereas approximate quantum many-body theories, when not based on a conserving approach, might give severely spurious results.

It should be remarked, however, that such reasonable mapping of a full quantum theory onto a phenomenological model is quite limited in the (Boltzmann) limit $\Gamma \ll \mu$. For the impurity scattering here considered, from Fig. 9(d) we roughly estimate (reminding the reader that $\hbar\omega_0 \approx \sqrt{3}\Gamma$) $\Gamma \sim 0.01\mu$,

corresponding here to $U \sim 0.015$. The origin of the breakdown of the model in Eq. (40) in describing correctly the purely intraband term spectral features and the dc limit can be traced in the relative evolution of the magnitude and energy scales of the purely intraband term versus the incoherent multiphoton transition edges, as shown in Fig. 10.

In the extreme weak-scattering limit [Fig. 10(a)] the pure intraband features, governed by the energy scale Γ , lie at energies much smaller than the multiphoton transition edges ruled by μ_0 , and they are thus well detached. The magnitude itself of the purely intraband term is also much bigger than the magnitude of the spectral features associated with the multiphoton edges, so that, as a result, the intraband part is essentially unaffected by the presence of the incoherent multiphoton features. In the intermediate regime $\Gamma \approx 0.1\mu$ [Fig. 10(b)] a purely intraband feature can still be identified, but, due to the large overlapping with the multiphoton edges (the smallest $n = 5$ lying at $\hbar\omega = 2\mu_0/5$), a reliable determination of its parameters, using Eq. (40) as a fitting guide, is not accessible. For further, larger scattering rates $\Gamma \gtrsim \mu$ [Fig. 10(c), see $U \geq 0.11$] the purely intraband spectral structures are essentially

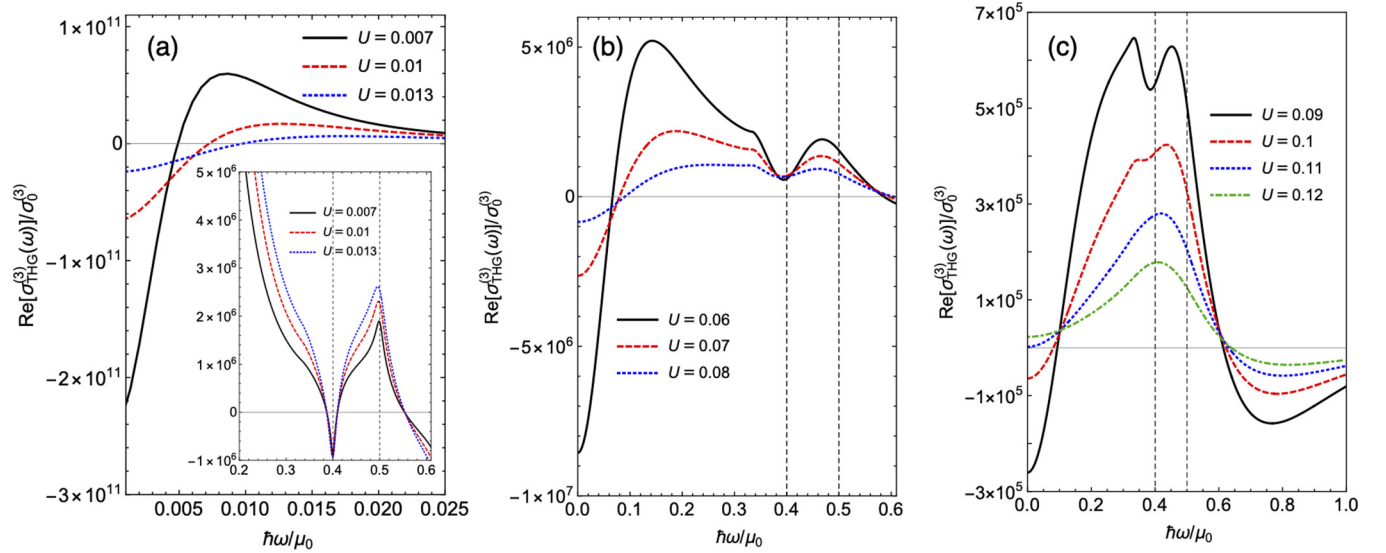


FIG. 10. Evolution of the real part of the THG conductivity for fixed chemical potential $\mu_0 = 25$ THz and varying the impurity scattering strength U , from the weak-scattering limit $\Gamma \ll \mu_0, \mu$ (a), to the intermediate crossover $\Gamma \approx 0.1\mu$ (b), to the strong-scattering regime $\Gamma \gtrsim \mu_0, \mu$ (c).

negligible, and the low-energy features are governed by the multiphoton transition edges with mixed intra- and interband character, resulting in a remarkable *change of sign* of the dc limit of the THG conductivity, consistent with the results of Ref. [18]. Figures 10(a)–10(c) display thus the evolution of the low-energy third harmonic generation from the high-doping (Boltzmann) regime to the quantum regime.

VI. SUMMARY AND CONCLUSION

In this paper we have explored the effects of the elastic impurity scattering on the third harmonic generation of graphene by using a conserving diagrammatic method that includes self-consistently both self-energy and vertex renormalization contributions. As a result of the field dependence of the self-energy, we showed that interaction-induced multiphoton vertex diagrams are relevant. In particular, we have predicted the onset of incoherent resonances at four- and five-photon transition energy with mixed intra- and interband character. Furthermore, we have shown that the main features of the purely intraband contribution in the full quantum theory are qualitatively comparable to phenomenological models that assume a frequency- and field-independent self-energy, whereas nonconserving approaches give rise to spurious results. In the terahertz regime the proximity of the five-photon transition edge at $\hbar\omega = 2\mu_0/5$ might affect the interpretation of experimental data in terms of a purely intraband term.

Our study sheds light on the importance of many-body interaction in qualitative explanations of nonlinear optics in the terahertz and infrared (intraband) regimes. Although the numerical study is performed for the third harmonic generation, the formalism is quite general and applicable to two-photon absorption, the nonlinear Kerr effect, etc. Moreover, our study can be simply generalized to explain the terahertz nonlinear response in other two-dimensional materials such as transition-metal dichalcogenides and twisted bilayer graphene.

ACKNOWLEDGMENT

H.R. acknowledges support from the Swedish Research Council (Grant No. VR 2018-04252).

APPENDIX A: RENORMALIZATION OF THE ONE-PHOTON VERTEX

The one-photon vertex renormalization is depicted diagrammatically in Fig. 4(a) of the main text, and it reads

$$\begin{aligned} \hat{\Lambda}_1(\mathbf{p}, \mathbf{p} + \mathbf{q}; n, n + m) &= \hat{\lambda}_1(\mathbf{p}, \mathbf{p} + \mathbf{q}; n, n + m) \\ &+ \gamma_{\text{imp}} \sum_{\mathbf{k}} \hat{G}(\mathbf{k}, n) \hat{\Lambda}_1(\mathbf{k}, \mathbf{k} \\ &+ \mathbf{q}; n, n + m) \hat{G}(\mathbf{k} + \mathbf{q}, n + m), \end{aligned} \quad (\text{A1})$$

where $m \equiv iq_m$ and $n \equiv ik_n = ip_n$ stand for the bosonic and fermionic Matsubara frequencies, respectively. Note that in the integrand we have shifted the dummy momentum \mathbf{k} as $\mathbf{k} + \mathbf{p} \rightarrow \mathbf{k}$, and therefore we can see that vertex correction does not depend on the fermion momentum \mathbf{p} . For the optical (or dipole) approximation we have $\mathbf{q} = \mathbf{0}$. Therefore the Bethe-Salpeter relation for the one-photon vertex function reads

$$\begin{aligned} \hat{\Lambda}_1(n, n + m) &= \hat{\lambda}_1(n, n + m) \\ &+ \gamma_{\text{imp}} \sum_{\mathbf{k}} \hat{G}(k, n) \hat{\Lambda}_1(n, n + m) \hat{G}(k, n + m). \end{aligned} \quad (\text{A2})$$

Note that we have $\hat{\lambda}_1(n, n + m) = \hat{\Lambda}_1^{(0)} = \delta \hat{G}_0^{-1} / \delta A|_{\mathbf{A} \rightarrow \mathbf{0}} = -e v \delta_y$, where \hat{G}_0 stands for the noninteracting Green's function. We assume the following ansatz for the vertex function:

$$\hat{\Lambda}_1(n, n + m) = a \hat{t} + b \sigma_x + (c + v) \sigma_y + d \sigma_z. \quad (\text{A3})$$

Using the fact that the integral of an odd function of \mathbf{k} is zero, we obtain $a = b = d = 0$ and eventually the following result for the vertex function: $\hat{\Lambda}_1 = (-ev\hat{\sigma}_y)\Lambda_1$ and $\hat{\lambda}_1 = (-ev\hat{\sigma}_y)\lambda_1$, where

$$\Lambda_1(n, n+m) = Q_1(n, n+m)\lambda_1. \quad (\text{A4})$$

Note that $\lambda_1 = 1$ and we define the one-photon vertex renormalization factor

$$Q_1(z, z') = \frac{1}{1 - UX_1(z, z')}, \quad (\text{A5})$$

in which

$$X_1(z, z') = \frac{\gamma_{\text{imp}}}{2U} \sum_{\mathbf{k}} \text{Tr}[\hat{\sigma}_y \hat{G}(\mathbf{k}, z) \hat{\sigma}_y \hat{G}(\mathbf{k}, z')]. \quad (\text{A6})$$

Using dimensional regularization, we find the following formula for the X_1 function:

$$X_1(z, z') = \frac{S(z)S(z')}{S(z)^2 - S(z')^2} \ln \left[\frac{S(z')^2}{S(z)^2} \right]. \quad (\text{A7})$$

Obviously, $X_1(z, z') = X_1(z', z)$.

APPENDIX B: RENORMALIZATION OF THE TWO-PHOTON VERTEX

Similar to the one-photon vertex case, it can be shown that the two-photon vertex function is independent of the fermionic momentum \mathbf{p} . Moreover, for the optical limit we can neglect the photon momentum \mathbf{q} . The self-consistent Bethe-Salpeter relation for the two-photon vertex function is depicted in Fig. 4(b) of the main text, and it reads

$$\begin{aligned} \hat{\Lambda}_2(n, n+m, n+2m) &= \hat{\lambda}_2(n, n+m, n+2m) \\ &+ \gamma_{\text{imp}} \sum_{\mathbf{k}} \hat{G}(\mathbf{k}, n) \hat{\Lambda}_2(n, n+m, n+2m) \hat{G}(\mathbf{k}, n+2m). \end{aligned} \quad (\text{B1})$$

In the noninteracting Dirac system the ‘‘bare’’ two-photon vertex function is zero, $\hat{\Lambda}_2^{(0)} \propto \delta^2 \hat{G}_0^{-1} / \delta A^2 |_{A \rightarrow 0} = 0$, due to the linear momentum dependence of the Hamiltonian. However, due to interaction the unrenormalized two-photon vertex $\hat{\lambda}_2$ is finite and is given by the following relation [see Fig. 5(a) of the main text]:

$$\begin{aligned} \hat{\lambda}_2(n, n+m, n+2m) &= -\gamma_{\text{imp}} \sum_{\mathbf{k}} \hat{G}(\mathbf{k}, n) \hat{\Lambda}_y(n, n+m) \\ &\times \hat{G}(\mathbf{k}, n+m) \hat{\Lambda}_y(n+m, n+2m) \hat{G}(\mathbf{k}, n+2m). \end{aligned} \quad (\text{B2})$$

From now on we adopt the shorthand notation $z_j = n + jm$ with $j = 0, 1, 2, 3$.

We find $\hat{\lambda}_2 = (-ev\hat{\sigma}_y)^2 \lambda_2$ with $\hat{\sigma}_y^2 = \hat{1}$ and

$$\lambda_2(z_0, z_1, z_2) = Q_1(z_0, z_1) Q_1(z_1, z_2) U Z(z_0, z_1, z_2), \quad (\text{B3})$$

in which $Q_1(z_i, z_j)$ is the one-photon renormalization factor defined in Appendix A and where

$$Z(z_0, z_1, z_2) = -\frac{\gamma_{\text{imp}}}{2U} \sum_{\mathbf{k}} \text{Tr}[\hat{G}(\mathbf{k}, z_0) \hat{\sigma}_y \hat{G}(\mathbf{k}, z_1) \hat{\sigma}_y \hat{G}(\mathbf{k}, z_2)]. \quad (\text{B4})$$

By performing the momentum integration using the dimensional regularization, we obtain

$$Z(z_0, z_1, z_2) = \frac{X_1(z_0, z_1) - X_1(z_1, z_2)}{S(z_0) - S(z_2)}. \quad (\text{B5})$$

By solving the the self-consistent Bethe-Salpeter relation for the two-photon vertex given in Eq. (B1), we obtain $\hat{\Lambda}_2 = (-ev\hat{\sigma}_y)^2 \Lambda_2$ with

$$\Lambda_2(z_0, z_1, z_2) = Q_2(z_0, z_2) \lambda_2(z_0, z_1, z_2), \quad (\text{B6})$$

in which $Q_2(z_0, z_2)$ is the two-photon Bethe-Salpeter renormalization factor

$$Q_2(z_0, z_2) = \frac{1}{1 - UX_2(z_0, z_2)} \quad (\text{B7})$$

and where

$$X_2(z, z') = \frac{\gamma_{\text{imp}}}{2U} \sum_{\mathbf{k}} \text{Tr}[\hat{G}(\mathbf{k}, z) \hat{G}(\mathbf{k}, z')]. \quad (\text{B8})$$

Therefore the two-photon renormalization factor reads

$$Q_2(z, z') = \frac{S(z) - S(z')}{z - z'}. \quad (\text{B9})$$

APPENDIX C: RENORMALIZATION OF THE THREE-PHOTON VERTEX

Similar to the two-photon case, the impurity scattering induces a finite three-photon vertex as defined in Fig. 5(b) of the main text. Accordingly, we find $\hat{\lambda}_3 = (-ev\hat{\sigma}_y)^3 \lambda_3$ with

$$\lambda_3(z_0, z_1, z_2, z_3) = \sum_{n=1}^3 M_n(z_0, z_1, z_2, z_3), \quad (\text{C1})$$

where

$$\begin{aligned} M_1(z_0, z_1, z_2, z_3) &= U \Omega_1(z_0, z_1, z_2, z_3) Q_1(z_0, z_1) \\ &\times Q_1(z_1, z_2) Q_1(z_2, z_3), \end{aligned} \quad (\text{C2})$$

$$\begin{aligned} M_2(z_0, z_1, z_2, z_3) &= U \Omega_2(z_0, z_2, z_3) \lambda_2(z_0, z_1, z_2) \\ &\times Q_1(z_2, z_3) Q_2(z_0, z_2), \end{aligned} \quad (\text{C3})$$

$$\begin{aligned} M_3(z_0, z_1, z_2, z_3) &= U \Omega_3(z_0, z_1, z_3) \lambda_2(z_1, z_2, z_3) \\ &\times Q_1(z_0, z_1) Q_2(z_1, z_3). \end{aligned} \quad (\text{C4})$$

Here, $Q_1(z_i, z_j)$ and $Q_2(z_i, z_j)$ are the Bethe-Salpeter one- and two-photon renormalization functions, respectively. The explicit expression for Ω_1 function is given by

$$\Omega_1(z_0, z_1, z_2, z_3) = \sum_{n=1}^3 u_n(z_0, z_1, z_2, z_3) \ln \left[\frac{S(z_0)^2}{S(z_n)^2} \right], \quad (\text{C5})$$

where we have

$$u_n(z_0, z_1, z_2, z_3) = \frac{\prod_j S(z_j) + R(z_0, z_1, z_2, z_3)S(z_n)^2}{\prod_{j \neq n} [S(z_n)^2 - S(z_j)^2]}, \quad (\text{C6})$$

in which $R(z_0, z_1, z_2, z_3) = S(z_0)S(z_2) + S(z_1)S(z_3)$. Similarly, by explicit calculation of the momentum integration, one

can obtain $\Omega_2(z_0, z_2, z_3) = Z(z_2, z_3, z_0)$ and $\Omega_3(z_0, z_1, z_3) = Z(z_3, z_0, z_1)$. Finally, the Bethe-Salpeter renormalization of the three-photon vertex function gives

$$\Lambda_3(z_0, z_1, z_2, z_3) = Q_3(z_0, z_3)\lambda_3(z_0, z_1, z_2, z_3), \quad (\text{C7})$$

where $Q_3(z_1, z_2) = Q_1(z_1, z_2)$.

-
- [1] J. L. Cheng, N. Vermeulen, and J. E. Sipe, *New J. Phys.* **16**, 053014 (2014).
- [2] J. L. Cheng, N. Vermeulen, and J. E. Sipe, *Phys. Rev. B* **91**, 235320 (2015).
- [3] S. A. Mikhailov, *Phys. Rev. B* **93**, 085403 (2016).
- [4] H. Rostami and M. Polini, *Phys. Rev. B* **93**, 161411(R) (2016).
- [5] H. Rostami and V. Juričić, *Phys. Rev. Research* **2**, 013069 (2020).
- [6] N. Kumar, J. Kumar, C. Gerstenkorn, R. Wang, H.-Y. Chiu, A. L. Smirl, and H. Zhao, *Phys. Rev. B* **87**, 121406(R) (2013).
- [7] R. I. Woodward, R. T. Murray, C. F. Phelan, R. E. P. de Oliveira, T. H. Runcorn, E. J. R. Kelleher, S. Li, E. C. de Oliveira, G. J. M. Fehine, G. Eda, and C. J. S. de Matos, *2D Mater.* **4**, 011006 (2016).
- [8] G. Soavi, G. Wang, H. Rostami, D. G. Purdie, D. De Fazio, T. Ma, B. Luo, J. Wang, A. K. Ott, D. Yoon, S. A. Bourelle, J. E. Muench, I. Goykhman, S. Dal Conte, M. Celebrano, A. Tomadin, M. Polini, G. Cerullo, and A. C. Ferrari, *Nat. Nanotechnol.* **13**, 583 (2018).
- [9] G. Soavi, G. Wang, H. Rostami, A. Tomadin, O. Balci, I. Paradisanos, E. A. A. Pogna, G. Cerullo, E. Lidorikis, M. Polini, and A. C. Ferrari, *ACS Photonics* **6**, 2841 (2019).
- [10] H. A. Hafez, S. Kovalev, J.-C. Deinert, Z. Mics, B. Green, N. Awari, M. Chen, S. Gernanskiy, U. Lehnert, J. Teichert, Z. Wang, K.-J. Tielrooij, Z. Liu, Z. Chen, A. Narita, K. Müllen, M. Bonn, M. Gensch, and D. Turchinovich, *Nature (London)* **561**, 507 (2018).
- [11] H. A. Hafez, S. Kovalev, K.-J. Tielrooij, M. Bonn, M. Gensch, and D. Turchinovich, *Adv. Opt. Mater.* **8**, 1900771 (2020).
- [12] Z. Mics, K.-J. Tielrooij, K. Parvez, S. A. Jensen, I. Ivanov, X. Feng, K. Müllen, M. Bonn, and D. Turchinovich, *Nat. Commun.* **6**, 7655 (2015).
- [13] S. A. Mikhailov, *Phys. Rev. B* **100**, 115416 (2019).
- [14] M. I. Katsnelson and A. I. Lichtenstein, *J. Phys.: Condens. Matter* **22**, 382201 (2010).
- [15] H. Rostami, M. I. Katsnelson, and M. Polini, *Phys. Rev. B* **95**, 035416 (2017).
- [16] A. Avdoshkin, V. Kozii, and J. E. Moore, *Phys. Rev. Lett.* **124**, 196603 (2020).
- [17] Z. Z. Du, C. M. Wang, H.-P. Sun, H.-Z. Lu, and X. C. Xie, [arXiv:2004.09742](https://arxiv.org/abs/2004.09742).
- [18] H. Rostami and E. Cappelluti, [arXiv:2007.08282](https://arxiv.org/abs/2007.08282) (accepted for publication in *NPJ 2D Mater. Appl.*).
- [19] Y.-W. Tan, Y. Zhang, K. Bolotin, Y. Zhao, S. Adam, E. H. Hwang, S. Das Sarma, H. L. Stormer, and P. Kim, *Phys. Rev. Lett.* **99**, 246803 (2007).
- [20] J. Horng, C.-F. Chen, B. Geng, C. Girit, Y. Zhang, Z. Hao, H. A. Bechtel, M. Martin, A. Zettl, M. F. Crommie, Y. R. Shen, and F. Wang, *Phys. Rev. B* **83**, 165113 (2011).
- [21] L. P. Kadanoff and G. Baym, *Quantum Statistical Mechanics* (CRC Press, Boca Raton, 1994).
- [22] G. Leibbrandt, *Rev. Mod. Phys.* **47**, 849 (1975).
- [23] M. E. Peskin, *An Introduction to Quantum Field Theory*, 1st ed. (CRC Press, Boca Raton, 1995).
- [24] A. H. Castro Neto, F. Guinea, N. M. R. Peres, K. S. Novoselov, and A. K. Geim, *Rev. Mod. Phys.* **81**, 109 (2009).
- [25] G. Baym and L. P. Kadanoff, *Phys. Rev.* **124**, 287 (1961).
- [26] L. P. Kadanoff and G. Baym, *Quantum Statistical Mechanics*, 1st ed. (Benjamin, New York, 1962).
- [27] N. H. Shon and T. Ando, *J. Phys. Soc. Jpn.* **67**, 2421 (1998).
- [28] A. Tsuneya, Y. Zheng, and S. Hidekatsu, *J. Phys. Soc. Jpn.* **71**, 1318 (2002).
- [29] H. Bruus and K. Flensberg, *Many-Body Quantum Theory in Condensed Matter Physics: An Introduction* (Oxford University Press, Oxford, 2017).